How dual-polarization radar observations can be used to verify model representation of secondary ice

Victoria A. Sinclair,[1] Dmitri Moisseev,[1,2] Annakaisa von Lerber,[2,3]

Corresponding author: Victoria Sinclair, Department of Physics , University of Helsinki, Finland. (victoria.sinclair@helsinki.fi)

[1]Department of Physics, University of Helsinki, Helsinki, Finland

[2]Finnish Meteorological Institute, Helsinki, Finland.

[3]School of Electrical Engineering, Aalto University, Finland.

Abstract. In this paper it is discussed how dual-polarization radar observations can be used to verify model representations of secondary ice production. An event where enhanced specific differential phase, K_{dp}, signatures in snow occur at the altitudes where temperatures lie in the range between -8 and -3 °C is investigated. By combining radar and surface-based precipitation observations it is shown that these dual-polarization radar signatures are most-likely caused by ice with concentrations exceeding those expected from primary ice parameterizations. It is also shown that the newly formed ice particles readily aggregate, which may explain why K_{dp} values seem to be capped at 0.2-0.3 °km^{-1} for a C-band radar. For the event of interest, multiple high resolution (1 km) Weather Research and Forecasting (WRF) model simulations are conducted. When the default versions of the Morrison microphysics schemes was used, the simulated number concentration of frozen hydrometeors is much lower than observed and the simulated ice particles concentrations are comparable with values expected from primary ice parameterizations. Higher ice concentrations, which exceed values expected from primary ice parameterizations, were simulated when ad-hoc thresholds for rain and cloud water mixing ratio in the Hallett-Mossop part of the Morrison scheme were removed. These results suggest that the parameterization of secondary ice production in operational weather prediction models needs to be re-visited and that dual-polarization radar observations, in conjunction with ancillary observations, can be used to verify them.

1. Introduction

Currently one of the major uncertainties in climate projections is due to feedbacks between clouds and radiation [*Webb et al.*, 2013; *Pachauri et al.*, 2014]. One reason for this is that detailed microphysical observations of cloud properties are still somewhat limited and thus microphysical parameterizations which are implemented in both weather prediction and climate models are difficult to verify [*Klein et al.*, 2013].

One of the longer standing challenges in microphysics is to account for the high number of ice particles observed relative to the number of ice nuclei. Several processes of ice multiplication have been suggested to explain this discrepancy. Shattering or partial fragmentation during the freezing of large supercooled drops is one such method [e.g. *Koenig*, 1963, 1965; *Rangno and Hobbs*, 2001]. A second potential method is spicule formation during the freezing of large drops. The spicules emit liquid bubbles that subsequently burst to produce multiple ice particles [e.g. *Rangno and Hobbs*, 2005; *Lawson et al.*, 2015]. A third potential mechanism of ice multiplication is the fragmentation of pre-existing ice particles due to ice particle-ice particle collisions [e.g. *Vardiman*, 1978; *Yano and Phillips*, 2011]. A fourth potential mechanism is the production of secondary ice during the evaporation of single particles including aggregates [*Beard*, 1992]. The final, most studied process, and the only secondary ice production process which is commonly included in operational weather prediction models, is rime splintering which is more commonly known as the Hallett-Mossop (H-M) process [*Hallett and Mossop*, 1974].

Hallett and Mossop [1974] conducted laboratory studies which showed that during the riming process ice splinters can be ejected during the freezing of supercooled liquid particles under certain conditions, namely at temperatures between -8°C and -3°C, and when liquid droplets with diameters greater than 25μm are present. However, few studies have shown any direct evidence of the H-M process occurring in the atmosphere. Recently, studies have shown circumstantial evidence which suggests the H-M process is occurring. For example, *Crawford et al.* [2012] combined aircraft observations, ground-based remote sensing and model simulations to identify ice formation processes. They concluded that secondary ice production via the H-M process was most likely active as in-situ observations showed small columnar crystals were present in the same sample volume as supercooled droplets and graupel, and that total ice number concentrations were far greater than what would be expected from primary ice production. In a similar study, *Crosier et al.* [2014] observed the "effects of ice multiplication" in a narrow cold front rainband and concluded that the H-M process was likely occurring as large ice particle number concentrations ($>$ 100 L^{-1}) were observed, the observed ice particles were columns, and the temperature was between -3 to -8°C. Both of these studies considered shallow convective clouds whereas in this study the focus is on stratiform frontal cloud bands that occurred in the cold season. Furthermore, while *Crawford et al.* [2012] and *Crosier et al.* [2014] relied heavily on in-situ aircraft data, in this study ground-based remote sensing and surface observations are considered which provide much longer time series of observations and more spatially expansive observations than aircraft based measurements.

The recent upgrade of many national weather radar networks to dual-polarization radar technology [*Doviak et al.*, 2000; *Bringi and Chandrasekar*, 2001] brings a new opportunity of using these state-of-the-art observations for documenting cloud and precipitation processes and for validating model parametrizations. *Hogan et al.* [2002] have presented measurements of embedded convection in a deep frontal ice cloud, where a region of enhanced differential reflectivity (Z_{dr}) coinciding with a turret of rising liquid water droplets was observed. They have advocated that the observed Z_{dr} is caused by needles formed by the H-M process. As the dual-polarization radar signature of newly formed needles is masked by that of graupel particles, which have much larger radar cross sections, the enhanced differential reflectivity values were observed in updrafts and not in the regions where the rime splintering process was taking place. Similar observations are reported by [*Giangrande et al.*, 2016]. *Oue et al.* [2015] used linear depolarization measurements at vertical incidence and Doppler spectra to detect columnar crystals and signatures of riming. They argued that, since the columnar crystals in their cases were formed at altitudes where temperatures lie in the range favorable for the H-M process to occur and that spectra show signatures of riming, the formed crystals are secondary ice produced by rime splintering. In both *Hogan et al.* [2002] and *Oue et al.* [2015], as is the case in most radar-based studies, the evidence presented for secondary ice production is circumstantial and mainly relies on the detection of newly formed ice particles at certain temperatures.

Grazioli et al. [2015] have reported that the enhanced K_{dp} signatures appear in regions where riming takes place and the production of ice needles is observed. They have argued that this may be an indication of the H-M process. *Kumjian et al.* [2016] have used this radar signature as an indicator for riming, given that it has to take place in the region where the H-M process is active. Thus, the aim of this study is to show that K_{dp} observations can identify regions where newly formed ice particles in the -3 to -8°C temperature region exceed those expected from primary ice parameterizations, and therefore, in conjunction with additional observations, can identify areas of secondary ice production. The second aim is to use these observations to ascertain if secondary ice production can be captured by a numerical weather prediction model and identify any limitations in the current parameterization of this process. In the case study presented here, dual-polarization radar observations are supplemented by microwave radiometer measurements, surface-based precipitation microphysics measurements and radiosonde soundings.

2. Data and Methods

In this study we analyze observations made at Hyytiälä, Finland (61°51'N,24°17'E, 181 m above sea level, Fig. 1) during the Biogenic Aerosols — Effects on Clouds and Climate (BAECC) campaign [*Petäjä et al.*, 2016] and combine these observations with results from a numerical weather prediction (NWP) model. The BAECC campaign took place between 1 February 2014 and 14 September 2014 during which time the United States Department of Energy's Atmospheric Radiation Measurement (ARM) Program ARM Mobile Facility (AMF2) was deployed to Hyytiälä. During the BAECC campaign an intensive observation period (IOP), termed the BAECC Snowfall Experiment (SNEX) focusing on snowfall, was undertaken from 1 February through 30 April 2014. During the BAECC-SNEX IOP, more than 20 snowfall events, where surface temperature was below 0°C were recorded. Using dual-polarization radar observations, eleven snowfall cases were identified as having elevated values of specific differential phase.

From these cases, three exhibited clear signatures at the height where air temperature ranged between -8 and -3°C. Model simulations of these three cases were conducted; however, for brevity, only the 15–16 February 2014 case is discussed here. This case is the simplest and is also the only case where the dual-polarization radar signatures took place just above ground – between the surface and a height of approximately 1.5 km – and hence surface-based precipitation microphysics measurements can be used to support the analysis.

2.1. Radar and microwave radiometer observations

Observations from two radars are used in this study: the Finnish Meteorological Institute Ikaalinen radar, which is a dual-polarized C-band weather radar [*Saltikoff et al.*, 2010], and the ARM Ka-band scanning cloud radar (Ka-SACR) [*Kollias et al.*, 2014a, b]. The Ikaalinen radar operates in simultaneous transmission and simultaneous reception mode [*Doviak et al.*, 2000]. Observations of equivalent reflectivity factor (Z_e), differential reflectivity (Z_{dr}) and specific differential phase (K_{dp}) are analyzed here. The radar is located 64 km east of the Hyytiälä site and performs range height indicator (RHI) scans over the site every 15 minutes and low-level (elevation angle 0.3°) plan position indicator (PPI) scans every 5 minutes. K_{dp} is calculated using the *Chanthavong et al.* [2010] implementation of the method proposed by *Wang and Chandrasekar* [2009].

The Ka-SACR performed a variety of scans during the BAECC experiment [*Kollias et al.*, 2014a]. On 15 Feb 2014 the radar was pointing vertically during the whole precipitation event and results from this event are presented in this paper. In addition to equivalent radar reflectivity, Ka-SACR measures linear depolarization ratio (LDR).

During BAECC the AMF2 instrumentation included two-channel (23.8 and 31.4 GHz) and three-channel (23.8, 30, and 89 GHz) microwave radiometers. From the measured brightness temperature, integrated water vapor and liquid water paths (LWP) are derived [*Cadeddu et al.*, 2013]. In this study, LWP data calculated from the two-channel microwave radiometer are used, though a comparison between the 2-channel and 3-channel radiometer LWP data showed little difference. The expected uncertainty in LWP estimates is about 0.02 kg m^{-2} [*Cadeddu et al.*, 2013].

2.2. Surface precipitation observations

The utilized surface precipitation instrumentation is part of the Global Precipitation Measurement (GPM) ground validation program of NASA. Analysis of the K_{dp} signatures is supported by ground-level observations of the microphysical properties of snow particles measured with NASA Particle Imaging Package (PIP), an improved version of the Snowflake Video Imager (SVI) [*Newman et al.*, 2009]. PIP records gray-scale images of the falling particles with a high frame-rate video camera as the particles fall in between the camera and an external light source. As PIP has a higher frame-rate than SVI, fall velocity measurements are possible even though the measurement volume of PIP is larger (field of view is 64 x 48 mm) than of SVI. All other particle image properties are obtained according to the SVI particle detection algorithm [*Newman et al.*, 2009]. PIP is located on the measurement field in Hyytiälä, approximately 50 m from the ARM AMF2 radars.

PIP particle data is recorded into 105 diameter bins with centers ranging from 0.125 to 26.125 mm. The measurements in the first bin are deemed unreliable and not used in the analysis. The disk equivalent diameter, D_{deq}, is defined as the diameter of a disk which has the same area as the measured area of the pixels included in the particle image, i.e. the total particle area. The particle size distribution (PSD) is recorded by PIP every minute and in this study the derived parameters — total particle concentration N_t, median volume diameter D_0 and maximum diameter D_{max} — are shown for five minute time periods. N_t and D_0 are calculated as follows:

$$N_t = \int_{D_{min}}^{D_{max}} N(D_{deq})\, \mathrm{d}D_{deq}, \tag{1}$$

$$\int_{D_{min}}^{D_0} D^3 N(D_{deq})\, \mathrm{d}D_{deq} = \int_{D_0}^{D_{max}} D^3 N(D_{deq})\, \mathrm{d}D_{deq} \tag{2}$$

where $N(D_{deq})$ is the PSD and D_{min} and D_{max} are minimum and maximum particle diameters used for the analysis. The single counts of questionable large particles are filtered before integrating over the mean distribution of five minutes for obtaining N_t. D_0 is also derived for the averaged distribution of five minutes, whereas D_{max} is the largest diameter observed during the five minute time period. The expected uncertainty of the retrieved PSD parameters is less than 10% but depends on the number of recorded particles during the observation period. Given that during the period of interest N_t did not change significantly, it is also expected that the uncertainty does not vary considerably in time either.

In addition to particle number concentrations, size, and velocity, information about particle shape is recorded. This includes parameters such as the dimensions of a bounding box, particle orientation angle, etc. From the bounding box dimensions and particle orientation, minor and major axes of the equivalent ellipse are calculated. The particle aspect ratio is defined as the ratio of the ellipse's minor and major axes. The area ratio is calculated from the measured total particle area and the area of a disk with the radius equal to major axis of the equivalent ellipse. It should be noted that because particle shape parameters, such as size, axis, and area ratios, are estimated from the two-dimensional projections they may differ from the true particle shape parameters as discussed, for example, by *Wood et al.* [2013]; *Tiira et al.* [2016].

Two weighing gauges are used to measure the liquid equivalent accumulation of the snow events. OTT Pluvio^2 200, with a collecting area of 200 cm^2 and a Tretyakov-type wind shield, is located at a height of 3 m inside a wind protection fence similar to the WMO standard Double-Fence Intercomparison Reference (DFIR) whereas OTT Pluvio^2 400, with collecting area of 400 cm^2 and both standard Alter- and Tretyakov-type wind protection shield [*Rasmussen et al.*, 2012], is placed on the field outside the wind fence. Both gauges agree well as, in addition to the wind fences, the Hyytiälä measurement field is sheltered by trees reducing under-catchment of the gauges because of the wind conditions. Accumulation data of the gauges is recorded every minute, but for comparison with model output, 10-minute accumulations are considered here.

The meteorological observations of temperature and surface pressure are measured by ARM meteorological tower instrumentation [*Kyrouac and Holdridge*, 2014] at a height of 10 m next to the ARM AMF2 radars. The archived data is averaged over 60 seconds but to enable fair comparison with model output, 10-minute averages are analyzed.

2.3. Weather Research and Forecasting (WRF) Model Simulations

Model simulations were conducted using version 3.6.1 of the Weather Research and Forecasting (WRF) model [*Skamarock et al.*, 2008]. WRF is a state-of-the-art, non-hydrostatic mesoscale Numerical Weather Prediction (NWP) model that is used extensively for both operational forecasting and research. WRF includes multiple parametrizations for each physical process (microphysics, boundary-layer turbulence etc.) which range in the level of complexity. In this study 36-hour simulations initialized using ERA-Interim reanalysis data [*Dee et al.*, 2011] are conducted starting approximately 12 hours before the time of interest to enable the model to spin-up. The simulations consist of an outer domain and three nested domains (Fig. 1); the outer domain has a horizontal grid spacing of 27 km which covers most of Europe, a second domain with a grid spacing of 9 km covering Northern Europe, a third domain with a grid spacing of 3 km covering Sweden, Norway, Finland and the Baltic countries and an inner nested domain with a grid spacing of 1 km which covers south and central Finland and the surrounding sea areas. The inner-most domain has 501 $\times$ 621 grid points and it is output from this inner domain which is analyzed and presented here. All domains have 60 model levels which results in a vertical grid spacing of less than 100 m in the boundary layer and approximately 300 m in the mid-troposphere. The simulations are conducted using the YSU boundary layer parameterization, the Kain-Fritsch cumulus convection scheme (only applied in the two outer domains), the RRTM longwave radiation scheme and the Dudhia short-wave radiation scheme.

The WRF simulations are conducted with the double-moment Morrison microphysics scheme [*Morrison et al.*, 2005] which predicts the mixing ratio of water vapor and five hydrometeor species (ice, snow, graupel, rain and cloud liquid) as well as the number concentration of ice, snow, graupel and rain particles. Secondary ice production due to rime-splinters is parameterized following *Hallett and Mossop* [1974]. For the H-M part of the parameterization to become active the temperature must be between -3°C and -8°C, graupel must be being produced, and the collection of cloud water by snow or the collection of snow by rain must also be occurring. An additional requirement is that the snow mixing ratio must exceed 0.1×10^{-3} kg kg^{-1} and that either the cloud water mixing ratio exceeds 0.5×10^{-3} kg kg^{-1} or that the rain mixing ratio exceeds 0.1×10^{-3} kg kg^{-1}. These ad-hoc values originate from *Lin et al.* [1983] and were also applied by *Rutledge* *and Hobbs* [1984]. In both of these earlier studies, these values were applied as thresholds for the production of graupel, not as thresholds for the activation of the H-M process as is the case in the Morrison microphysics scheme.

In addition to the control simulation with the default Morrison microphysics parameterization scheme, sensitivity experiments (see Table 1) were conducted to investigate the impact of the cloud water and rain mixing ratio thresholds in the H-M parameterization simply by removing these thresholds from the parameterization. Sensitivity experiments were also conducted to determine the impact of the parameterization of primary ice production. In the default Morrison scheme, the number of primary ice particles N_{pice} is parameterized using the Cooper curve [*Cooper*, 1986]

$$N_{pice} = 0.005 \exp\left(0.304\left(273.15 - T_k\right)\right) \tag{3}$$

where T_k is temperature in degrees Kelvin. In the sensitivity experiment, referred to as DeMott, the Cooper curve was replaced by

$$N_{pice} = 0.117 \exp\left(0.125\left(273.15 - T_k\right)\right) \tag{4}$$

which corresponds to the gray dashed line in Figure 2 of *DeMott et al.* [2010]. Note that this is not the parameterizaton proposed by *DeMott et al.* [2010] for ice nuclei concentration which is a function of number concentration of particles larger than 0.5μm diameter and temperature. Equation 4, subsequently referred to here as the "DeMott" curve, produces more ice particles than the Cooper curve at temperatures warmer than -17.5°C but fewer at colder temperatures. Finally, an experiment was conducted in which the production rate of ice due to the H-M process was multiplied by a factor of 10. A summary of the WRF experiments is given in Table 1.

3. Results

3.1. Synoptic Situation

At 12 UTC 15 February a mature occluded low pressure system with a central pressure of 964 hPa was centered over the North Sea. Associated with this system was a mature occluded front over the North Sea, southern Norway, and Denmark as well as a trailing cold front and a weak warm front to the south over Germany. Between 12 UTC 15 February and 00 UTC 16 February, this low pressure system and its fronts moved slowly north-east. By 00 UTC 16 February, the low was centered over western Norway and the occluded front, which was responsible for the precipitation analyzed in this study, was oriented North–South over western Finland (Fig. 1).

3.2. Signatures of secondary ice in radar and surface observations

At about 2345 UTC on February 15 a layer with enhanced K_{dp} values was observed above the Hyytiälä research station. These enhanced K_{dp} signatures appear as a localized area with a size of about 20 by 30 km in PPI measurements (Fig. 2) and as a layer in RHI observations (Fig. 3). The layer persisted for about an hour and extended from the ground to a height of 1.5 km as presented in Fig. 3. The K_{dp} values observed in the RHI scans directly above Hyytiälä were in the range 0.16 - 0.2 $^\circ$ km^{-1} with the highest values recorded at 0013 and 0028 UTC on February 16. It should be noted that values higher than 0.2 $^\circ$ km^{-1} were recorded in the PPI observations as shown in Fig. 2. At the same time and same heights, the Ka-SACR observations show enhanced values of LDR, which ranged between -25 and -21 dB. *Oue et al.* [2015] have reported that such LDR signatures observed at temperatures favoring rime splinter production can be potentially related to columnar crystals formed by the H-M process.

Unlike Z_{dr} and LDR, K_{dp} is not sensitive to spherical particles, such as lump graupel, or to low density particles, such as aggregates. Furthermore, K_{dp} is proportional to the number concentration of non-spherical dense particles, for example, needles. This makes K_{dp} a suitable tool for detecting areas of secondary ice production when used in conjunction with ancillary information, for example, temperature obtained from radiosonde soundings or model profiles. It should be noted that for accurate K_{dp} estimation, adequate radar signal is required.

Both K_{dp} and LDR observations indicate the presence of relatively dense non-spherical particles. The LDR observations from before 2330 UTC do show non-spherical particles that are falling out of a cirrus cloud layer (Fig. 3) to near the surface. At the time the K_{dp} signature is observed, the particles which are falling from above result in a lower LDR signal. However at the surface high LDR values are still observed. Because of the layer like appearance of the feature it is most probable that these particles were formed in the layer and did not originate from higher parts of the cloud. The radiosonde sounding (Fig. 4) shows that temperatures range between -3.5 and -5.5 °C in the layer and that air was saturated with respect to water. This indicates that ice crystals formed in this layer should be of the needle type. In addition, the relatively high temperatures observed in the layer of elevated K_{dp} values are unfavorable for primary ice production [e.g. *Cotton and Anthes*, 1989].

One of the main discriminators between primary and secondary ice is the number concentration. Based on parameterizations of primary ice applied in NWP models, the expected number concentration of primary ice particles formed in the observed layer range from $\sim 20\ m^{-3}$ to $200\ m^{-3}$, with the lower bound originating from the Cooper curve

(Eq. 3) and the upper values from the DeMott curve (Eq. 4). To verify whether this number concentration is sufficient to explain the observed K_{dp} bands scattering calculations were performed. The calculations were performed using Python based T-matrix code [*Leinonen*, 2014] that is based on earlier studies by *Mishchenko and Travis* [1994]; *Mishchenko et al.* [1996] and *Wielaard et al.* [1997]. The ice needles were modeled as prolate spheroids with refractive index defined by particle density using the Maxwell Garnett mixing rule [*Sihvola*, 1999]. There is an uncertainty related to the density of needles. *Heymsfield* [1972] have reported the density of needles (ρ) as a function of their length (L) in the form $\rho = 0.4583L^{-0.117}$, here centimeter-gram-second (cgs) units are used. In many other studies the density of needles was assumed to be one of pure ice, 0.9 g cm^{-3}. Since needles are modeled as prolate spheroids, axis ratios need to be assumed to perform the computations. To cover the range of possible axis ratio values [*Heymsfield*, 1972], computations were performed using values of 3, 5, 10 and 20. Since scattering properties of an ice particle are sensitive to the particle volume and the assumed axis ratio modifies the volume, the results will be affected by the axis ratio choice.

In Fig. 5 the calculated LDR and K_{dp} values, assuming that all ice crystals in the observation volume are the same size and that the total concentration is 1 m^{-3}, are shown. It can be seen that the assumed needle density has a significant effect on the computed values. In Fig. 5, minimum and maximum dimensions of the observed needles are depicted by circles, as was determined from the PIP observations. Since PIP diameter is the equivalent disk diameter, the transformation of this diameter to the needle length depends on an assumed axis ratio. For the observed range of needle sizes the minimum calculated K_{dp} value, assuming a crystal concentration of 1 m^{-3}, is just under 0.2×10^{-3} $^{\circ}km^{-1}$

and the maximum is $0.3 \times 10^{-3}\ ^{\circ}km^{-1}$, if density given by the *Heymsfield* [1972] relation is used. For the fixed density particles these values will be 0.5×10^{-3} and 0.87×10^{-3} $^{\circ}km^{-1}$, respectively. To convert these values to the ones expected from a population of primary ice, we should multiply these values by 200 m^{-3}, which is the total concentration of ice nuclei as given by the DeMott curve (Eq. 4) for a temperature of -5°C. This yields the range of expected K_{dp} values for the primary ice particles. If the *Heymsfield* [1972] density relation is assumed, the expected range is [0.04 - 0.06] $^{\circ}km^{-1}$, and for the fixed density needles it is [0.1 and - 0.18] $^{\circ}km^{-1}$. The range of K_{dp} values from the constant density assumption are close to the observed values. Therefore, the conclusion whether the K_{dp} signatures are indicative of primary or secondary ice depends on what assumption we make for particle density and, to a lesser extent, on which empirical relationship (e.g. the Cooper curve) we use to estimate the number of primary ice particles. The observed K_{dp} and LDR signatures can only be attributed to secondary ice if the *Heymsfield* [1972], or similar, density relation is valid. Growth instabilities observed at high supersaturations [*Nelson and Knight*, 1998] could be one reason why the needles observed here have lower densities than pure ice.

To support our radar based inferences, analysis of PIP observations was carried out. Firstly, observations show total concentrations of ice particles in the order of 10^4 m^{-3} at the surface (Fig. 6a). Further in-depth analysis is based on two approaches, visual inspection of recorded particle images as presented in [*Kneifel et al.*, 2015] and cluster analysis of velocity and particle shape observations. By examining the PIP video images recorded during the event on 15–16 February 2014, see Fig. 10 in *Kneifel et al.* [2015], it was noted that between 00 - 01 UTC multiple particle types were present. Especially between 0015 and 0045 UTC three particle types are clearly detectable. Indications of more than one particle type are also visible in velocity and area ratio measurements (Fig. 7c,d), which coincide with the times where increased K_{dp} values are observed (Fig. 7a,b). Both approaches show that prior to the high K_{dp} band being recorded (before 2330 - 2345 UTC 15 February), the surface observations showed only one population of particles which had typical fall velocities and area ratios of aggregates of moderately rimed dendrites.

To disentangle the contributions of the different particle habits to the total concentration a clustering analysis, assuming a three component Gaussian mixture model [*Mclachlan and Peel*, 2000], was performed. It is assumed that the PIP observations can be explained by the presence of three particle types, as was determined from the visual image analysis, and that each particle type corresponds to one of the multivariate Gaussian model densities. Observed diameters and fall velocities, computed areas and aspect ratios are used as inputs to the analysis. Parameters of multivariate Gaussian densities are optimized to maximize posterior probability, i.e. probability of data belonging to a certain cluster given observations of particle diameters, fall velocities, computed area and aspect ratios. Assignments of different clusters to particle types are done after the analysis was carried out using a qualitative assessment of the clusters characteristics. For example, slow falling non-spherical particles are treated as needles. The cluster analysis of the data yields total concentrations of respective particle types. It shows that there are about 2300 needles, 1500 needle aggregates and 2300 densely rimed assemblages of dendrites per cubic meter (Fig. 8). From this total concentration of needles, and the T-matrix calculations, we can conclude that the density relation proposed by *Heymsfield* [1972] is in better agreement with K_{dp} observations than the constant density assumption. Furthermore, the

IN concentration expected from empirical relationships ($\approx 200\ \mathrm{m}^{-3}$) is not large enough to explain the concentrations of needles observed at the surface. It should also be noted that a large portion of ice particles observed at the surface are needle aggregates. Therefore, the actual number of needles formed in the layer with elevated K_{dp} values would be higher, since a proportion of them are subsequently consumed in the aggregation process. By depleting needles, aggregation also caps the observed K_{dp} values. Another interesting aspect is the appearance of a large number of aggregates in this layer. *Moisseev et al.* [2015] have advocated that detectable K_{dp} values are associated with conditions favorable for the onset of aggregation. Even though their conclusion is based on analysis of K_{dp} bands that appear at temperatures close to -15 °C, it seems to hold here as well.

The analysis of dual-polarization radar and surface precipitation measurements support the initial hypothesis that the most probable mechanism responsible for formation of needles in this layer is the Hallett-Mossop rime splintering process. The K_{dp} layer appears at the right temperature range. The air is saturated with respect to water (Fig. 4) and furthermore, microwave radiometer observations show presence of supercooled liquid water (Fig. 9). The surface measurements of particles show the presence of heavily rimed particles needed for the onset of rime splintering process. The resulting total concentration of newly formed needles exceeds what is expected from primary ice parameterizations. A side product of this process is the formation of needle aggregates, which were observed on the ground and can also be seen in the observations of maximum particle diameter shown in Fig. 6b, which increases during the period when the secondary ice production is active.

3.3. Representation of secondary ice in WRF simulations

Figures 4 and 10 demonstrate that WRF simulates the large-scale structure of the frontal system reasonably well. The observed sounding at 00 UTC 16 February shows a saturated layer between 950 - 875 hPa, a slightly drier layer with a dewpoint depression of 2°C between 875-725 hPa and another shallow saturated layer between 725-700 hPa (Fig. 4). This structure is somewhat reproduced in the control WRF simulation. Two saturated layers (950-900 hPa and 825-775 hPa) separated by a drier layer are simulated which largely agrees with the observations. Above 700 hPa, the modeled dew point depression in the control WRF simulations is slightly smaller than observed suggesting that WRF has too much moisture in the mid-troposphere.

The modeled surface pressure, 2-m temperature and accumulated precipitation at the nearest grid box were compared to observations (Fig. 10). To ensure the validity of using the nearest grid box, values from the 100 surrounding grid boxes (in a 10 by 10 grid) were also analyzed (not shown). For precipitation and 2-m temperature variations were very small, whereas for surface pressure values varied by $\sim$5 hPa due to variations in the surface orography. The simulated surface pressure at the grid point closest to Hyytiälä, in both simulations, is lower than observed. However the simulated surface pressure at some of the nearby grid points agrees well with observations (not shown), as does the simulated rate of decrease of pressure (Fig. 10a). The simulated accumulated precipitation in the control WRF simulation is much lower than observed (Fig. 10b) but the timing of the onset and end of the precipitation are well captured indicating that WRF correctly captures the timing of the frontal passage. The simulated 2-m temperature differs somewhat from the observations, likely due to limitations in the boundary-layer parameterization scheme in stable conditions. However, the gradual warming associated with the passage of the front is captured relatively well (Fig. 10c).

The critical temperature levels for this study are -3°C and -8°C (indicated by the red isotherms in Fig. 4) which in the observed profile is the part of the atmosphere between 150 m (940 hPa) and 1.9 km (770 hPa). In the control simulation, the -3°C isotherm is about 150-200 m higher than observed and the -8°C isotherms is about 500 m higher. Therefore, the layer in which secondary ice production by the H-M process is possible is deeper, and extends higher, in the WRF simulation than in observations. A comparison between the observed and model simulated liquid water path (Fig. 9) demonstrates that WRF correctly simulated the amount of supercooled water in the vertical profile at the time the elevated K_{dp} signatures were observed. Therefore, WRF simulates the correct environmental conditions for the H-M process to occur and therefore it is viable to investigate the details of the simulated hydrometeors.

Height-time cross-sections of WRF simulated hydrometeors and temperature (Fig. 11) are analyzed to ascertain whether the control WRF simulation produces high ice number concentrations (N_{ice}) indicative of the H-M process. High number concentrations of ice particles are simulated at temperatures below -15°C (above ∼4 km, Fig. 11b). However, of more interest is the appearance of new ice particles below the -8°C level but above the -3°C level. In the control simulation, slightly higher ice number concentrations (maximum value of N_{ice} 23 m^{-3}) occur between 00 UTC and 01:30 UTC (Fig. 11b) than in the same temperature range at other times in the simulation. These ice particles are not formed by the H-M parametrization, as was confirmed by outputting the ice production tendencies from the H-M parameterization which were zero in this location (not shown).

It was hypothesized that the H-M parameterization did not become active as the Morrison scheme requires that either the cloud water or rain mixing ratio exceed certain thresholds (see section 2.3). This hypothesis was tested by performing additional experiments (No Thres, No Thres + DeMott and HM 10 – see Table 1 for explanations of experiment names) in which these ad-hoc thresholds were removed.

In No Thres (Fig. 12, left column) much higher ice number concentrations (maximum value, 5.3×10^3 m^{-3}) are simulated between 23:30 UTC and 00:00 UTC at $\sim$2 km and also between 0015 UTC and 02 UTC at lower levels than in the control simulation. The model calculated ice number production tendencies due to the H-M process (not shown) confirm that ice was produced due to the H-M parameterization between 2310 and 2345 UTC. In contrast, the high ice number concentrations simulated at lower levels after 00 UTC were not co-located with high ice number production tendencies due to the H-M process. However, the enhanced ice concentrations simulated at low level after 00 UTC in No Thres must be associated with the production of secondary ice by the H-M process. In HM10, (Fig. 12, right column) even higher ice concentrations (maximum value, 4.9 $\times\ 10^4$ m^{-3}) are simulated both between 2330 UTC and 00 UTC and between 0015 UTC and 02 UTC.

When the primary ice parameterization was changed to the DeMott curve (see supplementary material), removing the ad-hoc cloud water and rain mixing ratio thresholds from the H-M parameterization had the same affect as when the Cooper curve was used: higher ice concentrations were observed at low levels. In the DeMott + No Thres experiment, ice concentrations of approximately 10^3m^{-3} are simulated at 0030 UTC at 1 km.

A fair comparison between model-simulated ice particle concentrations and those inferred from K_{dp} observations or measured at the surface is challenging. Firstly, K_{dp} based estimates only account for non-spherical particles. Secondly, the surface PIP observations only measure particles with diameters larger than 0.375 mm and therefore may underestimate the actual total particle number concentration. Finally, while WRF simulates multiple hydrometeor species, observations measure all frozen hydrometeors together. A comparison between the observed particle number concentrations at the surface and the sum of the model simulated frozen hydrometeor — ice, snow and graupel — concentrations, N_{ice}, N_{snow} and $N_{graupel}$ respectively, at the lowest model level ($\approx$ 40 m a.g.l., Fig. 13a) shows that all model simulations underestimate the number concentrations between 23 and 01 UTC. During this time, the No Thres and HM10 simulations agree best with observations, however, these simulations may still be under-estimating the total concentration of frozen hydrometeors as the PIP observations are potentially negatively biased as small particles are not measured. However, Fig. 13a also shows that when the ad-hoc rain and cloud water mixing ratio thresholds are removed, the simulations over-estimate the number concentrations after 02 UTC.

K_{dp} observations imply that about 10^3 m^{-3} non-spherical particles were present at 0030 between the surface and 1 km. High K_{dp} values were also observed earlier at 2343 at 2 – 2.5 km (Fig. 3). In both the control and DeMott simulations, the model simulated frozen hydrometeors number concentrations at 2330 UTC and at model level 6 ($\approx$0.63 km, Fig. 13b) are approximately 400 m^{-3}. Higher concentrations are found in No Thres and HM10 at 2330 UTC. At 0030 UTC, the control and DeMott simulations have almost an order of magnitude fewer frozen hydrometeors than estimated from K_{dp} observations whereas better agreement is found between both No Thres and DeMott + No Thres and observations. Thus, regardless of which primary ice parameterization is used, removing the thresholds of rain and cloud mixing ratio leads to a significant increase in number concentration, and consequently, much better agreement with observations.

The impact of changing the number concentration of ice particles on the accumulated surface precipitation was investigated to determine if the representation of secondary ice production in NWP models could be one source of errors in precipitation forecasts. Removing the rain and cloud water mixing ratio thresholds in both No Thres and DeMott + No Thres had very little impact on surface precipitation (Fig. 13c), yet when the H-M production rates were multiplied by 10, accumulated precipitation increased by 10%. However, the primary ice parameterization also had an impact on the accumulated precipitation with approximately 14% more precipitation occurring when the Cooper curve was used compared to the DeMott curve (Fig. 13c).

4. Conclusions

In this study we have investigated how dual-polarization radar observations, in combination with detailed surface-based observation of precipitation microphysical properties, can be used to evaluate the representation of secondary ice in WRF, a numerical weather prediction model. Observations obtained during the BAECC-SNEX campaign are analyzed and high-resolution WRF simulations were conducted. The focus of this paper was one snowfall event which occurred on 15–16 February 2014 that had an layer of elevated K_{dp} values between the surface and 1.5 km.

This study has shown that K_{dp} observations enable the detection and characterization of zones where secondary ice production may be active when combined with ancillary observations and scattering calculations. Scattering calculations in which LDR and K_{dp} for ice crystals with dimensions suggested by the PIP observations and a concentration of 1 m^{-3} were performed thus allowing estimates of number concentrations to be obtained from the observed K_{dp} values. It was shown that if the density of needles is assumed to be given by the *Heymsfield* [1972] equation, then the number of primary ice particles estimated using empirical relationships that are applied in primary ice parameterizations, is too low to explain the observed K_{dp} values. However, if a constant needle density is assumed, the observed K_{dp} values potentially could be explained by the presence of primary ice. Thus, the assumption for density is critical.

The PIP observations show that three types of particles were observed: small needles, aggregates and rimed particles. Rimed particles are required for the H-M process to occur, the small needles are an expected product of the H-M process and the aggregates are thought to form from the newly produced needles. The onset of aggregation of the newly formed ice particles may explain why K_{dp} values seem to be capped at 0.2-0.3 $^{\circ}$km^{-1}. In addition, the PIP observations show that an order of magnitude more needles are observed at the surface than primary ice parametrizations would account for.

The surface-based and dual-polarization radar observational results presented in this paper do suggest that a secondary ice production process is occurring. However, it is exceedingly difficult to prove without any doubt that that process is the Hallett-Mossop process even though considerable circumstantial evidence exists. Thus, a caveat in using these observations to validate microphysical schemes is that since the H-M process is the only secondary ice production method included in the Morrision microphysics scheme, if the observed secondary ice particles are produced by an alternative process, then the

WRF simulations should not be expected to simulate ice concentrations similar to those observed. However, given the large amount of evidence, i.e. the presence of supercooled water and of graupel-like particles, the correct temperature range, we propose that the secondary ice was produced by the H-M process and thus validate the WRF simulations based on this.

Comparisons between the observed and modeled bulk meteorological variables and the concentration and mixing ratios of hydrometeors were conducted. Firstly, the control WRF simulation was able to realistically reproduce the timing of the frontal system, the thermodynamic vertical structure of the atmosphere and the vertically integrated liquid water path. However, the control simulation underestimated the precipitation rate and the number of ice particles present in the -3°C and -8°C layer despite accurately simulating the amount of supercooled water and graupel. Additional sensitivity experiments suggested that the underestimation of ice particles in the -3 to -8°C layer is at least partly due to the ad-hoc thresholds of rain and cloud mixing ratios: either the cloud water mixing ratio must exceed 0.5×10^{-3} kg kg^{-1} or the rain mixing ratio must exceeds 0.1×10^{-3} kg kg^{-1} for the H-M part of the Morrison microphysics parameterization to become active. These results suggest that these ad-hoc thresholds should be reconsidered, and their applicability to high-latitude mixed phase clouds be scrutinized.

The cause of the underestimation of the precipitation rate is unclear and may be due to inaccuracies in the large-scale thermodynamic structure of the atmosphere or due to the misrepresentation of microphysical processes. Increasing the number of ice particles produced by the H-M process by multiplying the production rate by a factor of 10 increased the precipitation amount by $\sim$ 10% whereas removing the rain and cloud water mixing ratio thresholds did not have any impact on accumulated precipitation. This suggests that only when very high ice concentrations are produced by the H-M process, aggregation of the newly formed particles can enhance surface precipitation.

In conclusion, this study has indicated that dual-polarization radar observations, which are now available from operational radars, can be used to detect zones where secondary ice production may take place. Further, we have shown an example of how the representation of secondary ice in microphysical parameterization schemes can be verified using a combination of dual polarization radar observations, detailed surface precipitation observations and scattering calculations. The results of this study suggest that current NWP models which include double moment microphysics schemes and a parameterization of the H-M processes cannot realistically represent secondary ice. This conclusion is based on results from one model and one microphysics scheme and only one case study has been presented here. Therefore, the validity of these results should be further investigated. However, doing so is challenging due to the limited observations of the required level of detail that are currently available. Therefore, we suggest that long-term detailed microphysical measurements of surface precipitation are conducted in conjunction with dual-polarization radar observation. Such measurements would enable advancement of secondary ice parameterizations.

Acknowledgments. We acknowledge the work of the Hyytiälä station and ARM AMF2 personnel for the daily tasks with measurements, especially mentioning Matti Leskinen and Janne Levula. We would like to thank Susanna Lautaportti for the help in selecting the cases. We thank the NASA GPM ground validation program and Dr. Walter Petersen for providing ground-based precipitation instrumentation used in this study. The research of DM was supported by Academy of Finland (grant 263333). DM and VAS were also supported by the Academy of Finland Finnish Center of Excellence program (grant 272041). AvL was funded by grant of the Vilho, Yrjö and Kalle Väisälä Foundation. The radar and meteorological data from the BAECC campaign used in this study are available from the ARM data archive at http://www.archive.arm.gov. We acknowledge CSC–IT Center for Science Ltd for the allocation of computational resources which enabled us to perform the WRF simulations.

References

Barthazy, E., and R. Schefold (2006), Fall velocity of snowflakes of different riming degree and crystal types, *Atmos. Res.*, *82*, 391–398, doi:10.1016/j.atmosres.2005.12.009.

Beard, K. V. (1992), Ice initiation in warm-base convective clouds: An assessment of microphysical mechanisms, *Atmospheric research*, *28*(2), 125–152.

Bringi, V. N., and V. Chandrasekar (Eds.) (2001), *Polarimetric Doppler Weather Radar*, 636 pp., Cambridge Univ. Press, New York.

Cadeddu, M. P., J. C. Liljegren, and D. D. Turner (2013), The Atmospheric Radiation Measurement (ARM) program network of microwave radiometers: instrumentation, data, and retrievals, *Atmos. Meas. Tech.*, *6*(9), 2359–2372, doi:10.5194/amt-6-2359-2013.

Chanthavong, V., J. Holmes, R. Kernen, S. Panov, J. Selzler, T. Stordell, and V. Chandrasekar (2010), Operational implementation of the adaptive specific differential phase, in *Proc. Sixth European Conf. on Radar in Meteorology and Hydrology*, ERAD.

Cooper, W. A. (1986), *Precipitation Enhancement—A Scientific Challenge*, chap. Ice Initiation in Natural Clouds, pp. 29–32, American Meteorological Society, Boston, MA, doi:10.1007/978-1-935704-17-1_4.

Cotton, W. R., and R. A. Anthes (1989), *Storm and Cloud Dynamics*, Academic Press.

Crawford, I., et al. (2012), Ice formation and development in aged, wintertime cumulus over the UK: observations and modelling, *Atmos. Chem. Phys.*, *12*(11), 4963–4985.

Crosier, J., et al. (2014), Microphysical properties of cold frontal rainbands, *Q. J. R. Meteorol. Soc.*, *140*(681), 1257–1268.

Dee, D. P., et al. (2011), The ERA-Interim reanalysis: Configuration and performance of the data assimilation system, *Q. J. R. Meteorol. Soc.*, *137*(656), 553–597.

DeMott, P. J., A. J. Prenni, X. Liu, S. M. Kreidenweis, M. D. Petters, C. H. Twohy, M. Richardson, T. Eidhammer, and D. Rogers (2010), Predicting global atmospheric ice nuclei distributions and their impacts on climate, *Proceedings of the National Academy of Sciences*, *107*(25), 11,217–11,222.

Doviak, R., V. Bringi, A. Ryzhkov, A. Zahrai, and D. Zrnic (2000), Considerations for polarimetric upgrades to operational WSR-88D radars, *J. Atmos. Oceanic Technol.*, *17*(3), 257–278.

Giangrande, S. E., T. Toto, A. Bansemer, M. R. Kumjian, S. Mishra, and A. V. Ryzhkov (2016), Insights into riming and aggregation processes as revealed by aircraft, radar, and disdrometer observations for a 27 april 2011 widespread precipitation event, *Journal of Geophysical Research: Atmospheres*, *121*(10), 5846–5863, doi:10.1002/2015JD024537, 2015JD024537.

Grazioli, J., G. Lloyd, L. Panziera, C. R. Hoyle, P. J. Connolly, J. Henneberger, and A. Berne (2015), Polarimetric radar and in situ observations of riming and snowfall microphysics during CLACE 2014, *Atmospheric Chemistry and Physics*, *15*(23), 13,787–13,802, doi:10.5194/acp-15-13787-2015.

Hallett, J., and S. C. Mossop (1974), Production of secondary ice particles during the riming process, *Nature*, *249*, 26–28.

Heymsfield, A. (1972), Ice crystal terminal velocities, *J. Atmos. Sci.*, *29*, 1348–1357.

Hogan, R. J., P. R. Field, A. J. Illingworth, R. J. Cotton, and T. W. Choularton (2002), Properties of embedded convection in warm-frontal mixed-phase cloud from aircraft and polarimetric radar, *Q. J. R. Meteorol. Soc.*, *128*(580), 451–476, doi:10.1256/003590002321042054.

Klein, S. A., Y. Zhang, M. D. Zelinka, R. Pincus, J. Boyle, and P. J. Gleckler (2013), Are climate model simulations of clouds improving? An evaluation using the ISCCP simulator, *J. Geophys. Res.*, *118*(3), 1329–1342.

Kneifel, S., A. von Lerber, J. Tiira, D. Moisseev, P. Kollias, and J. Leinonen (2015), Observed relations between snowfall microphysics and triple-frequency radar measurements, *J. Geophys. Res.*, *120*(12), 6034–6055, doi:10.1002/2015JD023156, 2015JD023156.

Koenig, L. R. (1963), The glaciating behavior of small cumulonimbus clouds, *J. Atmos. Sci.*, *20*(1), 29–47.

Koenig, L. R. (1965), Drop freezing through drop breakup, *J. Atmos. Sci.*, *22*(4), 448–451.

Kollias, P., N. Bharadwaj, K. Widener, I. Jo, and K. Johnson (2014a), Scanning ARM Cloud Radars. Part I: Operational Sampling Strategies, *J. Atmos. Oceanic Technol.*, *31*(3), 569–582, doi:10.1175/JTECH-D-13-00044.1.

Kollias, P., I. Jo, P. Borque, A. Tatarevic, K. Lamer, N. Bharadwaj, K. Widener, K. Johnson, and E. E. Clothiaux (2014b), Scanning ARM Cloud Radars. Part II: Data Quality Control and Processing, *J. Atmos. Oceanic Technol.*, *31*(3), 583–598, doi:10.1175/JTECH-D-13-00045.1.

Kumjian, M. R., S. Mishra, S. E. Giangrande, T. Toto, A. V. Ryzhkov, and A. Bansemer (2016), Polarimetric radar and aircraft observations of saggy bright bands during MC3E, *Journal of Geophysical Research: Atmospheres*, *121*(7), 3584–3607, doi: 10.1002/2015JD024446, 2015JD024446.

Kyrouac, J., and D. Holdridge (2014), ARM Surface Meteorological Instrumentation (MET), http://www.archive.arm.gov/discovery/#v/home/s/, doi:10.5439/1025220.

Lawson, R. P., S. Woods, and H. Morrison (2015), The microphysics of ice and precipitation development in tropical cumulus clouds, *J. Atmos. Sci.*, *72*(6), 2429–2445.

Leinonen, J. (2014), High-level interface to t-matrix scattering calculations: architecture, capabilities and limitations, *Opt. Express*, *22*(2), 1655–1660, doi:10.1364/OE.22.001655.

Lin, Y.-L., R. D. Farley, and H. D. Orville (1983), Bulk parameterization of the snow field in a cloud model, *J. Climate Appl. Meteor.*, *22*(6), 1065–1092.

Locatelli, J., and P. Hobbs (1974), Fall speeds and masses of solid precipitation particles, *J. Geophys. Res.*, *79*(15), 2185–2197, doi:10.1029/JC079i015p02185.

Mclachlan, G., and D. Peel (Eds.) (2000), *Finite Mixture Models*, John Wiley & Sons, Inc., Hoboken, NJ, doi:10.1002/0471721182.ch1.

Mishchenko, M. I., and L. D. Travis (1994), T-matrix computations of light scattering by large spheroidal particles, *Optics Communications*, *109*(1), 16 – 21, doi:10.1016/0030-4018(94)90731-5.

Mishchenko, M. I., L. D. Travis, and A. Macke (1996), Scattering of light by polydisperse, randomly oriented, finite circular cylinders, *Appl. Opt.*, *35*(24), 4927–4940, doi:10.1364/AO.35.004927.

Moisseev, D. N., S. Lautaportti, J. Tyynela, and S. Lim (2015), Dual-polarization radar signatures in snowstorms: Role of snowflake aggregation, *J. Geophys. Res.*, *120*(24), 12,644–12,655, doi:10.1002/2015JD023884, 2015JD023884.

Morrison, H., J. A. Curry, and V. I. Khvorostyanov (2005), A new double-moment microphysics parameterization for application in cloud and climate models. Part I: Description, *J. Atmos. Sci.*, *62*(6), 1665–1677.

Nelson, J., and C. Knight (1998), Snow crystal habit changes explained by layer nucleation, *J. Atmos. Sci.*, *55*(8), 1452–1465.

Newman, A., P. Kucera, and L. Bliven (2009), Presenting the snowflake video imager (SVI), *J. Atmos. Oceanic Technol.*, doi:10.1175/2008JTECHA1148.1.

Oue, M., M. R. Kumjian, Y. Lu, J. Verlinde, K. Aydin, and E. E. Clothiaux (2015), Linear depolarization ratios of columnar ice crystals in a deep precipitating system over the Arctic observed by zenith-pointing Ka-Band Doppler radar, *J. Appl. Meteorol. Climatol.*, *54*(5), 1060–1068.

Pachauri, R. K., et al. (2014), Climate Change 2014: Synthesis Report. Contribution of Working Groups I, II and III to the Fifth Assessment Report of the Intergovernmental Panel on Climate Change. Intergovernmental Panel on Climate Change.

Petäjä, T., et al. (2016), BAECC a field campaign to elucidate the impact of Biogenic Aerosols on Clouds and Climate, *Bulletin of the American Meteorological Society*, doi: 10.1175/BAMS-D-14-00199.1.

Rangno, A. L., and P. V. Hobbs (2001), Ice particles in stratiform clouds in the Arctic and possible mechanisms for the production of high ice concentrations, *J. Geophys. Res.*, *106*, 15.

Rangno, A. L., and P. V. Hobbs (2005), Microstructures and precipitation development in cumulus and small cumulonimbus clouds over the warm pool of the tropical Pacific Ocean, *Q. J. R. Meteorol. Soc.*, *131*(606), 639–673.

Rasmussen, R., et al. (2012), How well are we measuring snow: The NOAA/FAA/NCAR winter precipitation test bed, *Bull. Amer. Meteor. Soc.*, *93*, 811829.

Rutledge, S. A., and P. V. Hobbs (1984), The mesoscale and microscale structure and organization of clouds and precipitation in midlatitude cyclones. XII: A diagnostic modeling study of precipitation development in narrow cold-frontal rainbands, *J. Atmos. Sci.*, *41*(20), 2949–2972.

Saltikoff, E., A. Huuskonen, H. Hohti, J. Koistinen, and H. Järvinen (2010), Quality assurance in the FMI doppler weather radar network, *Boreal Environ. Res.*, *15*(6), 579–594.

Sihvola, A. (1999), *Electromagnetic mixing formulas and applications*, London : Institution of Electrical Engineers.

Skamarock, W. C., J. B. Klemp, J. Dudhia, D. O. Gill, D. M. Barker, X.-Y. Huang, W. Wang, and J. G. Powers (2008), A description of the Advanced Research WRF Version 3, *Tech. Rep. NCAR/TN-475+STR*, NCAR.

Tiira, J., D. N. Moisseev, A. von Lerber, D. Ori, A. Tokay, L. F. Bliven, and W. Petersen (2016), Ensemble mean density and its connection to other microphysical properties of falling snow as observed in southern finland, *Atmospheric Measurement Techniques Discussions*, *2016*, 1–29, doi:10.5194/amt-2016-192.

Vardiman, L. (1978), The generation of secondary ice particles in clouds by crystal-crystal collision, *J. Atmos. Sci.*, *35*(11), 2168–2180.

Wang, Y., and V. Chandrasekar (2009), Algorithm for estimation of the specific differential phase, *J. Atmos. Oceanic Technol.*, *26*(12), 2565–2578, doi:http://dx.doi.org/10.1175/2009JTECHA1358.1.

Webb, M. J., F. H. Lambert, and J. M. Gregory (2013), Origins of differences in climate sensitivity, forcing and feedback in climate models, *Climate dynamics*, *40*(3-4), 677–707.

Wielaard, D. J., M. I. Mishchenko, A. Macke, and B. E. Carlson (1997), Improved t-matrix computations for large, nonabsorbing and weakly absorbing nonspherical particles and comparison with geometrical-optics approximation, *Appl. Opt.*, *36*(18), 4305–4313, doi:10.1364/AO.36.004305.

Wood, N. B., T. S. L'Ecuyer, F. L. Bliven, and G. L. Stephens (2013), Characterization of video disdrometer uncertainties and impacts on estimates of snowfall rate and radar reflectivity, *Atmospheric Measurement Techniques*, *6*(12), 3635–3648, doi:10.5194/amt-6-3635-2013.

Yano, J.-I., and V. T. J. Phillips (2011), Ice-ice collisions: An ice multiplication process in atmospheric clouds, *J. Atmos. Sci.*, *68*(2), 322–333.

Table 1. Summary of experiments conducted with WRF. In HM10, the production rate of ice particles due to the H-M processes is multiplied by a factor of 10.

Exp. Name	Microphyics scheme	Primary Ice parameterization	Q_{rain} / Q_{cloud} thresholds
Control	Morrison	Cooper curve	on
DeMott	Morrison	DeMott curve	on
No Thres	Morrison	Cooper curve	off
DeMott + No Thres	Morrison	DeMott curve	off
HM10	Morrison	Cooper curve	off

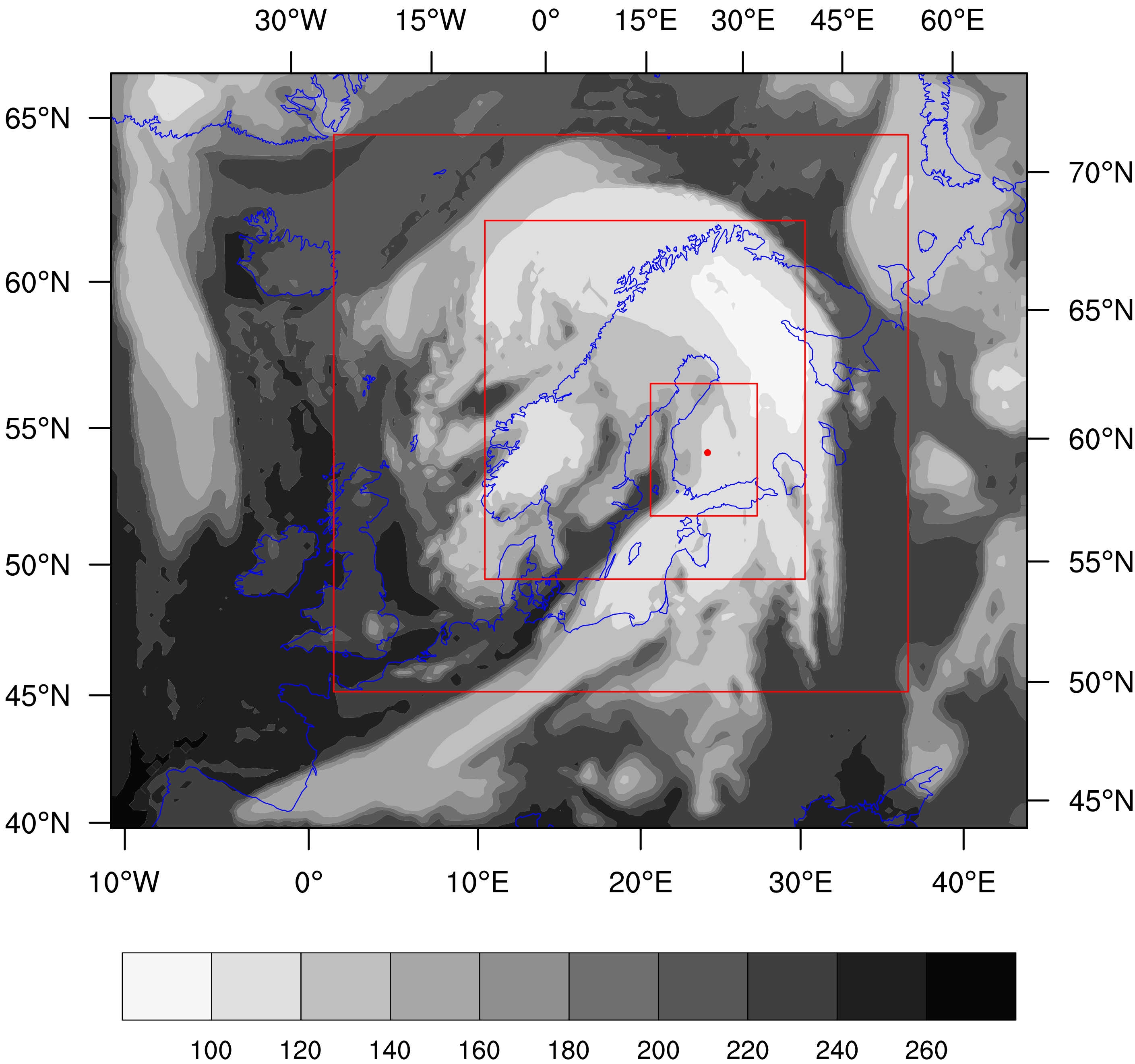

Figure 1. Map showing the outer model domain (whole map) and the three nested domains (red boxes), the location of Hyytiälä field station (red dot) and the model simulated outgoing long wave radiation (shading, W m^{-2}) from the outermost domain (d01) at 00 UTC 16 February 2014.

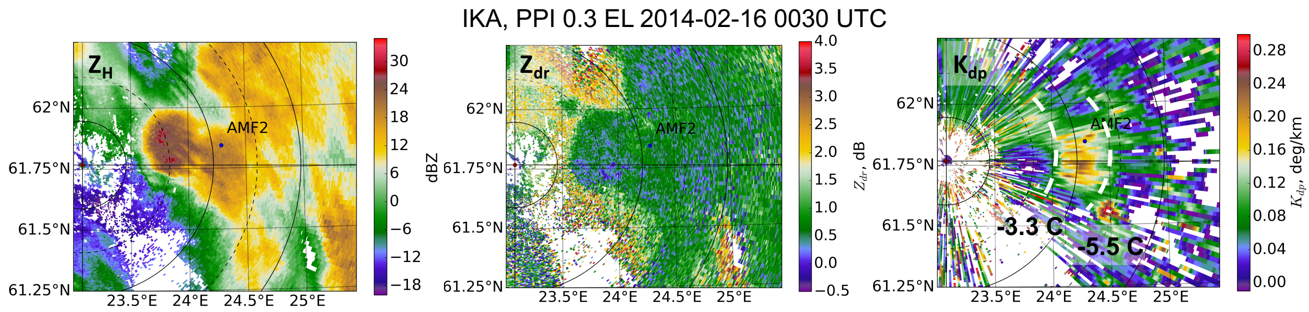

Figure 2. Ikaalinen radar plan position indicator (PPI) observations of equivalent reflectivity factor, differential reflectivity and specific differential phase recorded on Feb. 16, 2014 at 0030 UTC. The radar elevation angle is 0.3°. The 20 km range rings are shown in the figure. The temperature labels correspond to range arcs (white dashed curves), depicting boundaries of the K_{dp} band.

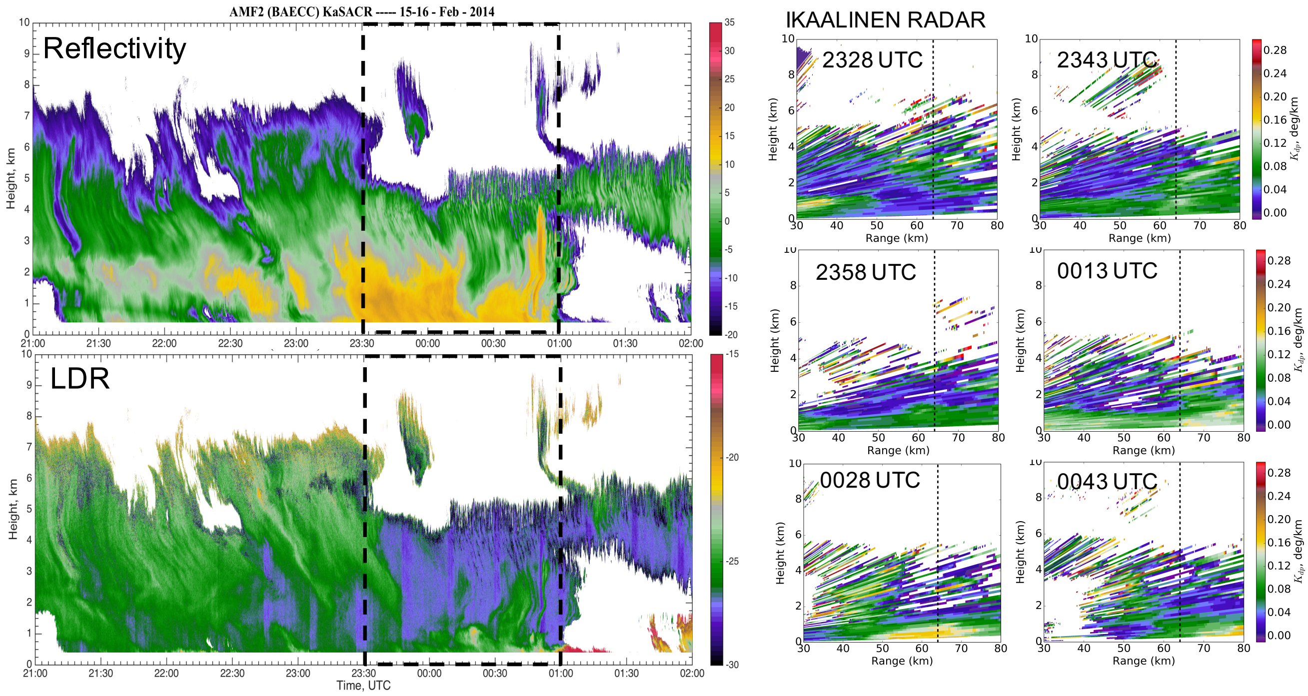

Figure 3. Ikaalinen radar RHI observations of specific differential phase and Ka-SACR vertical pointing observations of equivalent reflectivity factor and linear depolarization ratio. The K_{dp} band was observed between 2330 UTC and 0100 UTC, highlighted by a dashed black line box in the time-height figures of K_{dp} and LDR. The RHI observations are carried out over the Hyytiälä field station, azimuth 81.9 °. The dashed line in the RHI images indicate profiles above the measurement station.

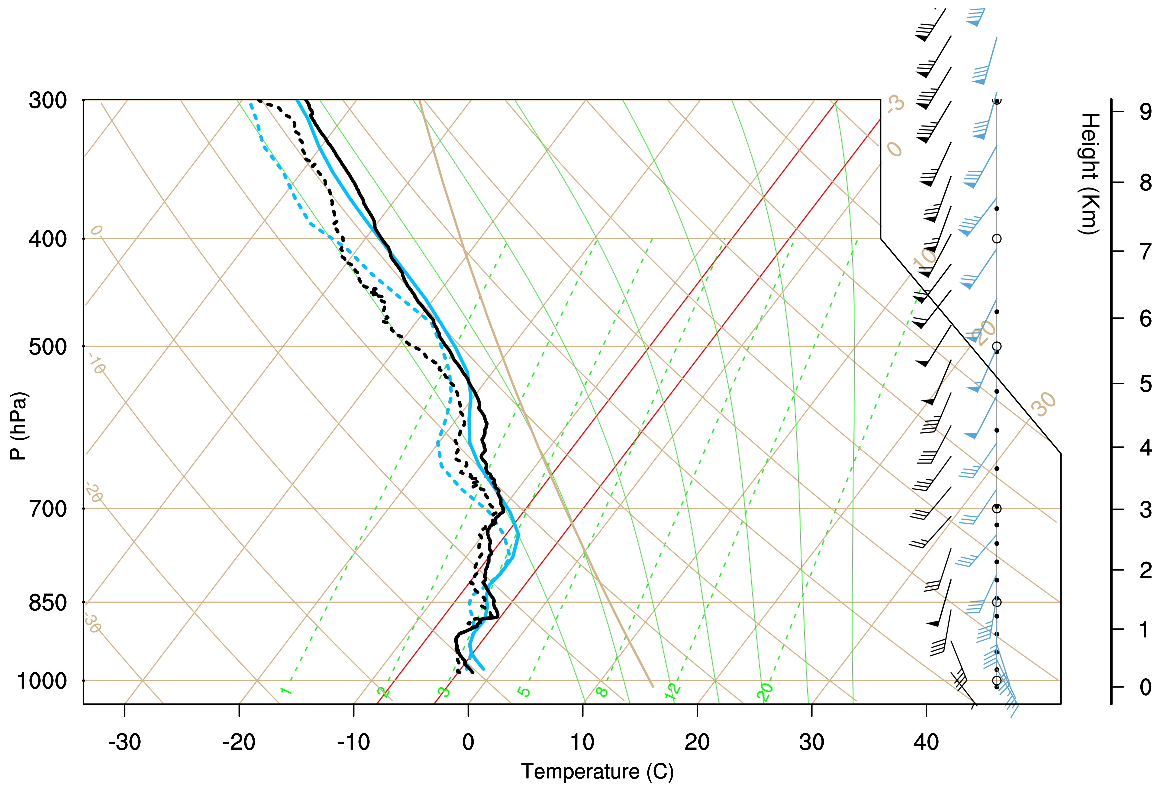

Figure 4. Skew-T diagram showing observations (black) and model output (blue) at 00 UTC 16 February 2014 from the control simulation. Solid lines show temperature profiles and dashed lines dewpoint temperatures. Wind barbs are plotted every at 2nd model level and every 50th observation.

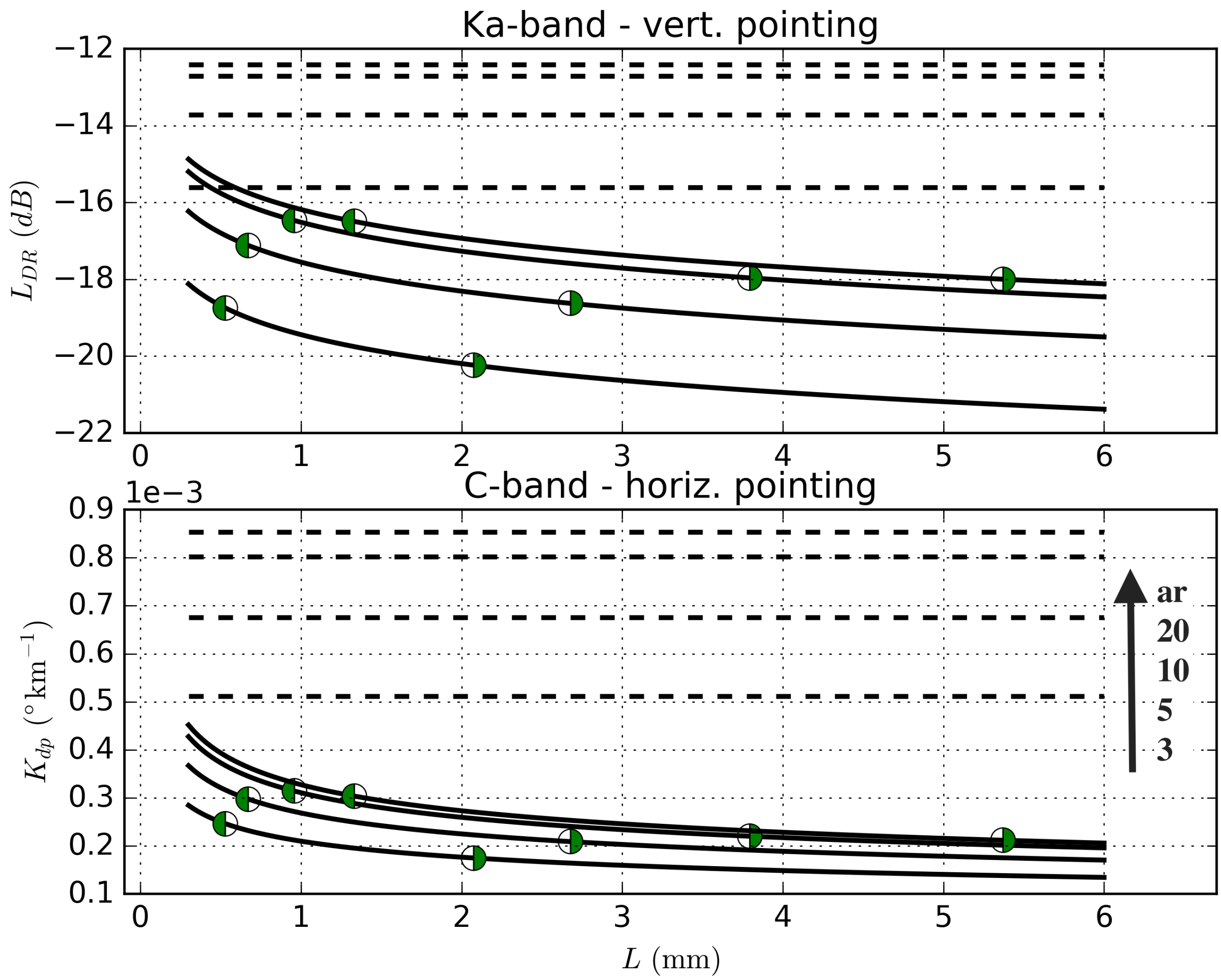

Figure 5. K_{dp} and LDR calculations for needles as a function of length (L) and axis ratio (ar). K_{dp} calculations are done for C-band assuming that crystal concentration is 1 m^{-3}. The LDR computations are for vertically pointing Ka-band radar. Standard deviation of 10° is assumed for particle canting angles and uniform distribution for the azimuth angles. Solid lines represent calculations using the *Heymsfield* [1972] density relation for 4 different axis ratios (3, 5, 10 and 20) as indicated by the solid black arrow. Dashed lines depict calculations using constant density of 0.9 g cm^{-3} for these 4 axis ratios. The circles show minimum and maximum lengths of needles as calculated from PIP observations.

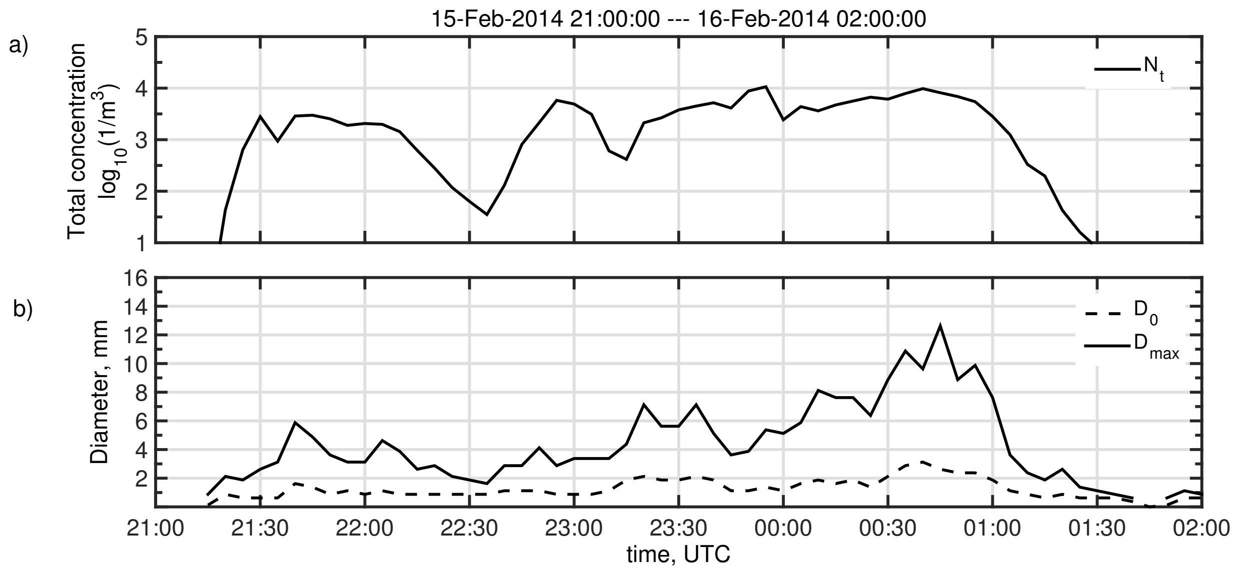

Figure 6. Time series of (a) the total number concentration N_t, (b) the median volume diameter D_0 and the maximum particle diameter D_{max} observed by PIP between 2100 UTC on February 15 and 0200 UTC on February 16.

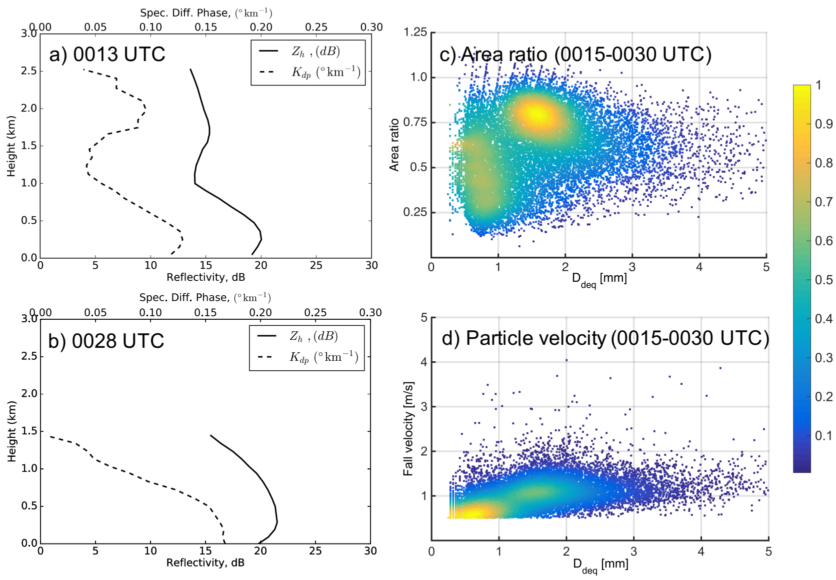

Figure 7. Ikaalinen radar recorded profiles of Z_e and K_{dp} above the measurement site a)-b) and corresponding observations shown as density plots of c) ice particle area ratios and d) fall velocities as a function of diameter. The color of the density plot represent the normalized density, which is ranging from 0 to 1 as shown in the colorbar.

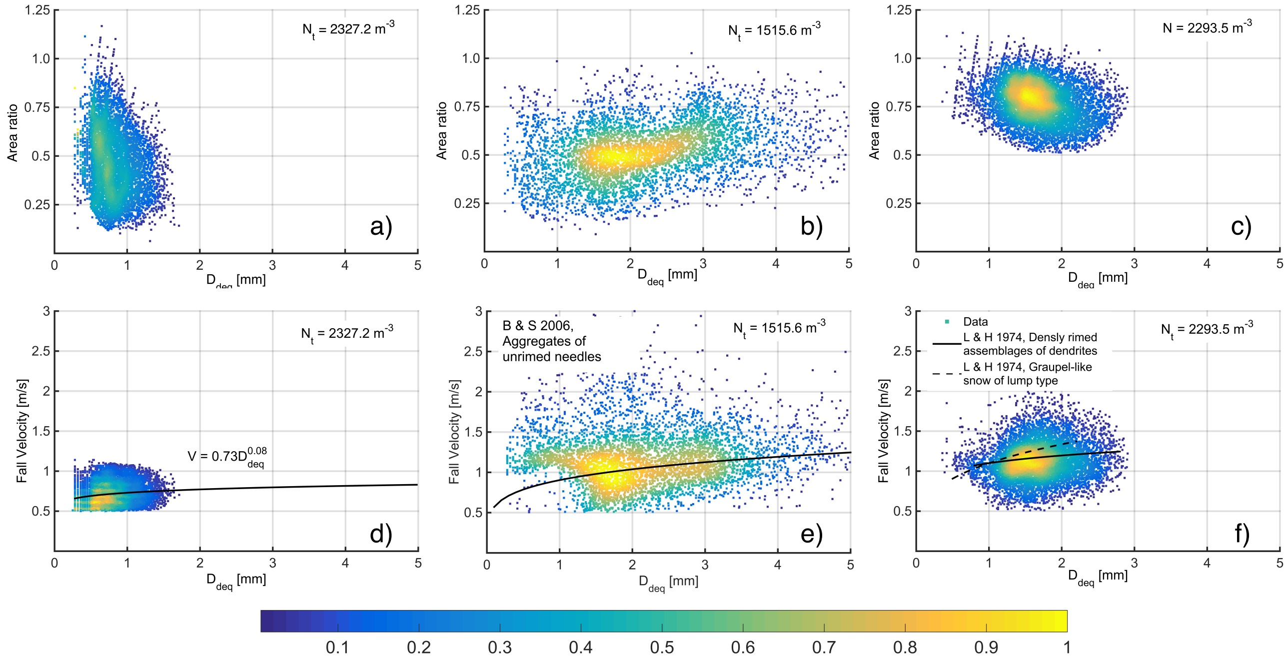

Figure 8. Density plots of retrieved area ratios and observed fall velocities of the three particle types as functions of diameter with the estimated number concentrations separated by a clustering algorithm valid at the same time as Fig 7c, d. Small needle-like particles are shown in a) and d) with V-D relation defined with nonlinear regression. Aggregates are depicted in b) and e), and the V-D relation is taken from *Barthazy and Schefold* [2006] with a pressure correction based on the measurement heights with respect to mean sea level. c) and f) are the area ratios and fall velocities, respectively, as function of diameter for rimed particles and the V-D relations for densely rimed assemblages of dendrites and graupel-like snow of lump type are taken from *Locatelli and Hobbs* [1974].

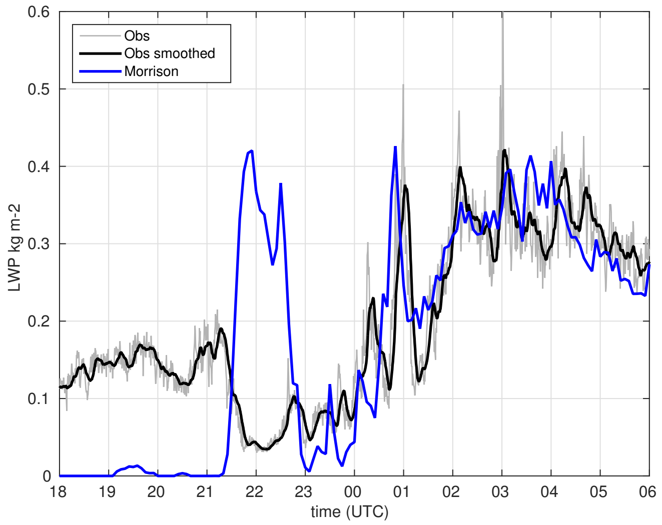

Figure 9. Observed liquid water path (gray), observed liquid water path smoothed using a 10-minute running mean (black) and the model simulated liquid water path (blue) from the control simulation.

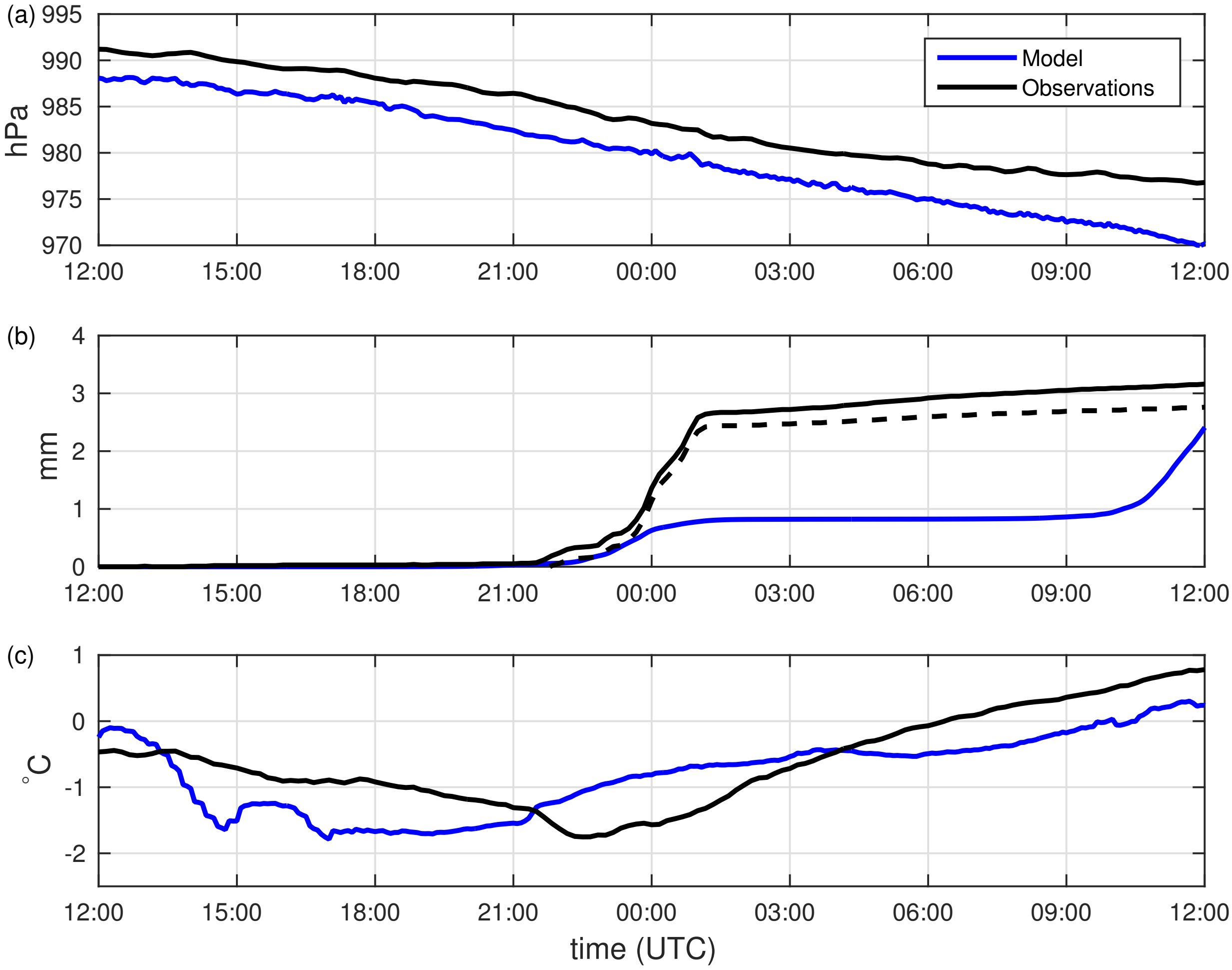

Figure 10. Time series of (a) surface pressure, (b) accumulated precipitation and (c) 2-m temperature. Black lines show observations, blue lines the output from the control WRF simulation. All model variables are from the grid box closest to Hyytiälä. In (b) the solid black line is for measurements inside of the snow fence and the dashed line for measurements outside of the snow fence.

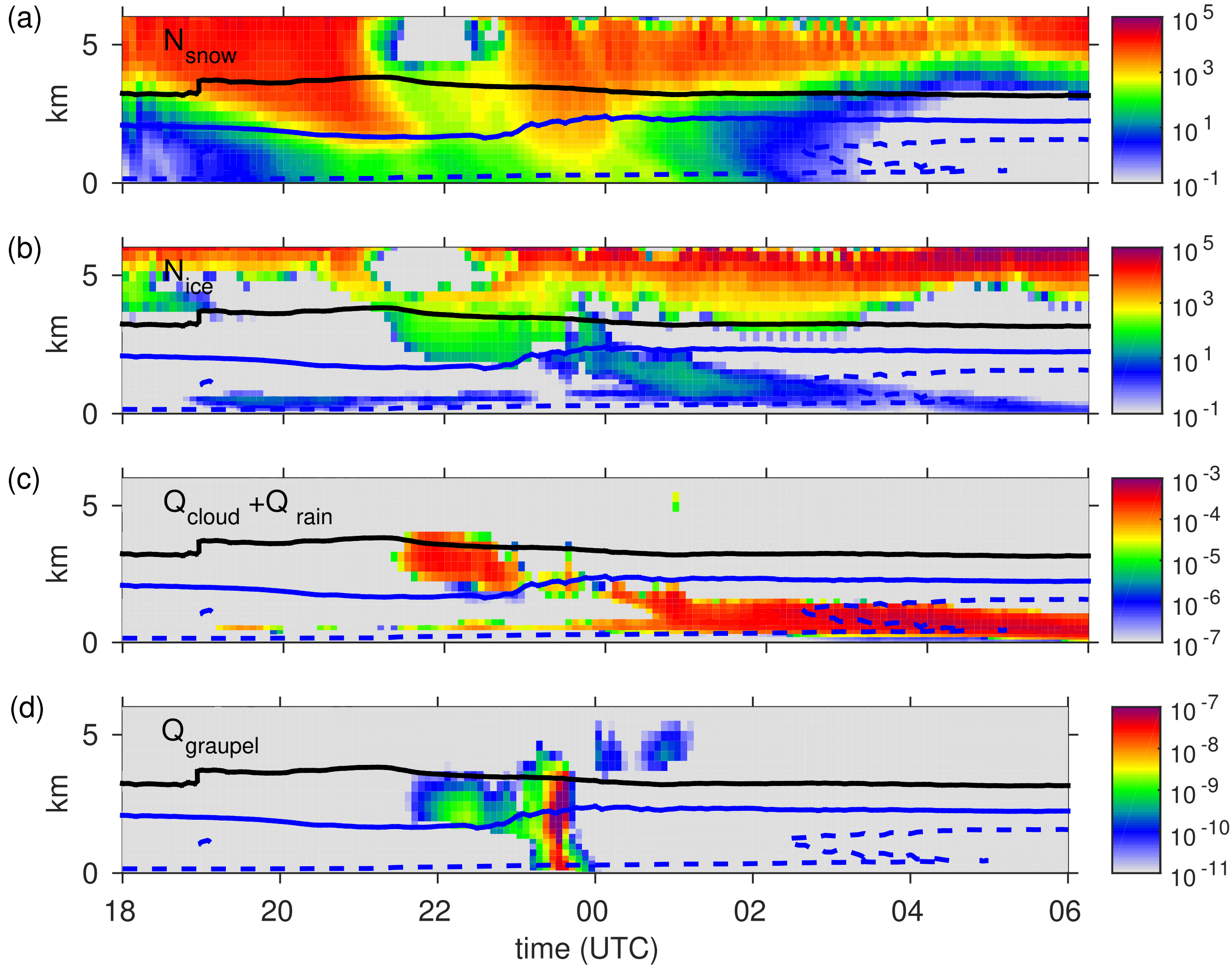

Figure 11. Model simulated hydrometeors (shading) and temperature (contours) from the control simulation at the grid point closest to Hyytiälä between 18 UTC 15 February 2014 and 06 UTC 16 February 2014. (a) number concentration of snow particles (N_{snow}), (b) number concentration of cloud ice particles (N_{ice}), (c) sum of the cloud liquid and rain mixing ratio (Q_{cloud}+Q_{rain}) and (d) graupel mixing ratio ($Q_{graupel}$). Units in panels a–b are m^{-3} and kg m^{-3} in panel c–d. The black solid line show -15°C, the blue solid line -8°C, and the blue dashed line -3°C. Note that color bars differ between panels.

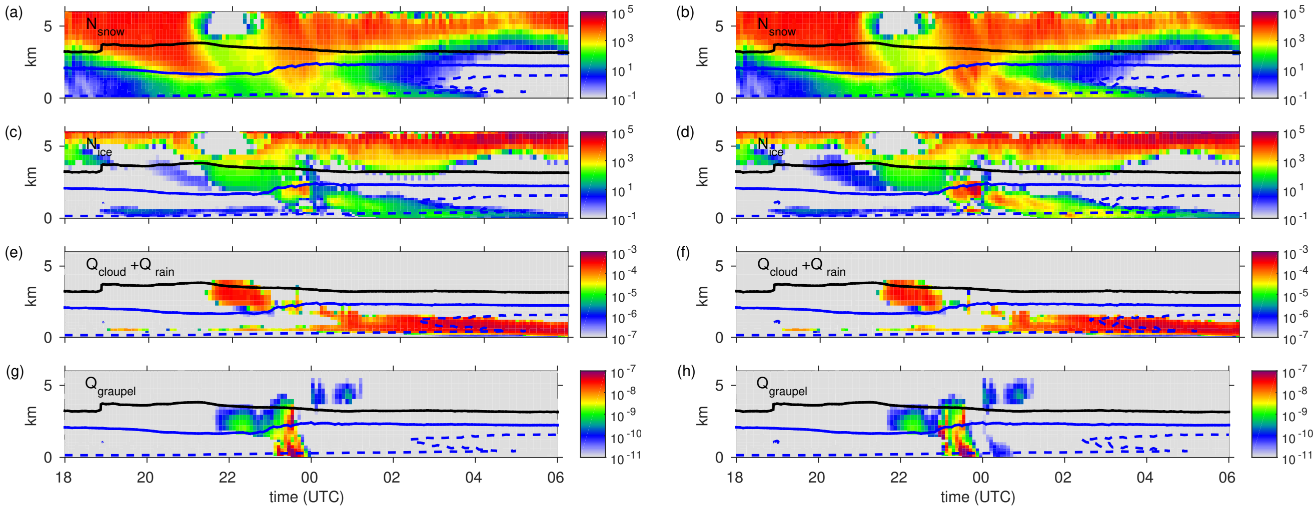

Figure 12. Model simulated hydrometeors (shading) and temperature (contours) in experiment No Thres (left) and HM10 (right). (a,b) number concentration of snow particles (N_{snow}), (c,d) number concentration of ice particles (N_{ice}), (e,f) sum of the cloud liquid and rain mixing ratio (Q_{cloud}+Q_{rain}) and (g,h) graupel mixing ratio ($Q_{graupel}$). Units in panels a–d are m^{-3} and kg m^{-3} in panel e–h. The black solid line show -15°C, the blue solid line -8°C, and the blue dashed line -3°C. Note that color bars differ between panels.

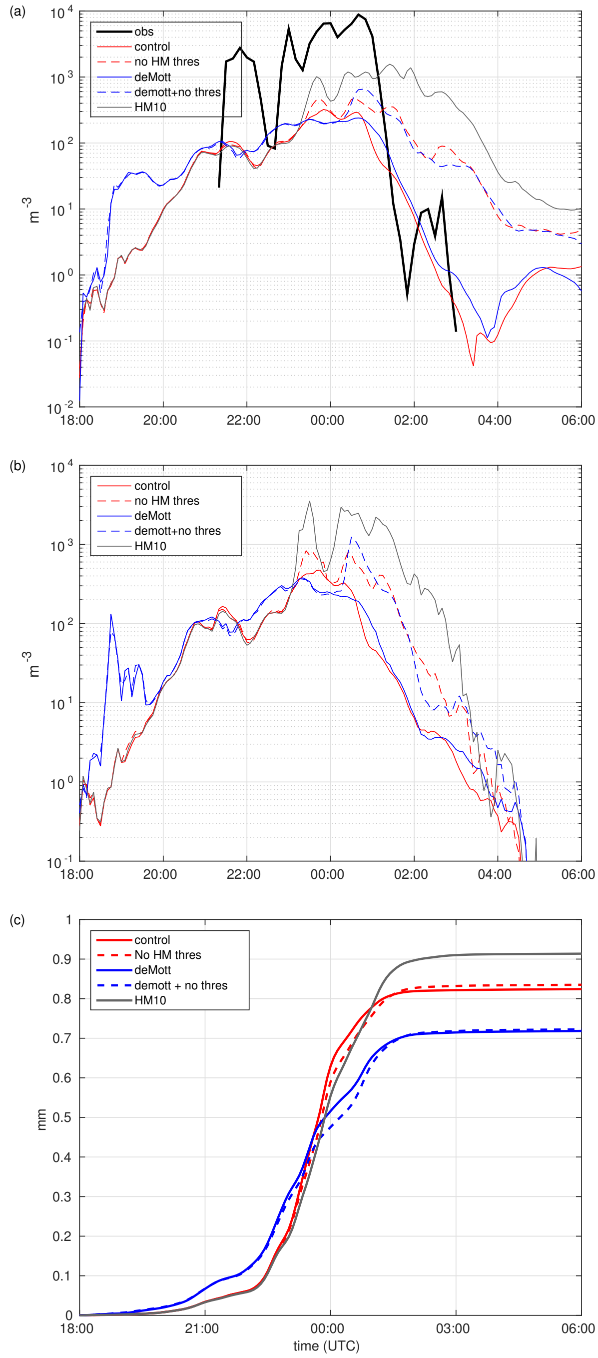

Figure 13. (a,b) Number concentration of the sum of all frozen particles (N_{ice}, N_{snow} and $N_{graupel}$) at (a) the lowest model level (approximately 40 m) and (b) at model level 6 (approximately 0.63 km). (c) model simulated accumulated precipitation. Red: control simulation, Red dashed: No Thres, Blue: DeMott, Blue dashed: DeMott + No Thres, Grey: HM10. Solid black line in (a) shows total number concentration observed by PIP.